# Basic Study on Velocity Control in Wing Coordinate System Using Acceleration-based Disturbance Observer for Tilt-wing eVTOL

Takuma Katagiri* Student Member, Kentaro Yokota** Non-member
Kota Fujimoto* Student Member, Sakahisa Nagai* Member
Hiroshi Fujimoto*a) Senior Member

Recently, the development of electric Vertical Take-off and Landing (eVTOL) has attracted much attention thanks to their promising application in various scenarios of human society, such as new means of transportation, surveillance, and dangerous place inspection. A tilt-wing eVTOL is one of the most promising type because of its small wing drag during ascend and the ability to use the propeller slipstream during transition. We propose a novel velocity control system in wing coordinate system with acceleration-based disturbance observer for a tilt-wing eVTOL. Our proposed method has the merits for a disturbance rejection and decoupling control. To evaluate the effectiveness of these merits, computer simulations and Hardware-In-the-Loop simulations using a wind tunnel is conducted.

**Keywords:** tilt-wing, eVTOL, velocity control, disturbance observer

## 1. Introduction

**1.1 Background of eVTOL** Vertical Take-off and Landing (VTOL) has been developed since the 1900s because of its advantage of not requiring a runway for take-off and landing. In recent years, electric VTOL (eVTOL) has attracted great attention because of the technology developments such as high-performance batteries, electric propulsion technology, and automatic driving technology [(1)] to provide a new means of transportation or to play roles in monitoring and surveillance in dangerous places. To realize an eVTOL system, electric propulsion technology is especially a key technology. It has the advantages of fast torque response and quick thrust control [(2)], which provides accurate torque estimation and enables us to power regeneration [(3)]. Taking advantage of these capabilities, we have been studying new control method such as airspeed estimation using motor current measurements [(4)], and fast and efficient thrust control of variable-pitch-propeller [(5)].

There are two types of eVTOLs: fixed-wing type and rotary-wing type. This paper focuses on the fixed-wing type eVTOL which can fly longer distance than the rotary-wing type. Among fixed-wing type eVTOLs, the tilt-wing type is superior in terms of a smaller drag force on the wings than tilt-rotor type during ascent because the wings face upward. In addition, it can use the propeller slipstream during transition. In this paper, we focus on tilt-wing eVTOL because of these advantages.

**1.2 Literature review on tilt-wing eVTOL** The tilt-wing eVTOLs are prone to become unstable during transitions because the aerodynamic characteristics are significantly changed by tilting the wing angle. To cope with this problem, many studies have been conducted on attitude control and velocity control [(6)~(8)].

In Ref. (6), a controller was designed for a tandem tilt-wing aircraft to stabilize the flight for both longitudinal and lateral-directional motions. It shows a complete transition from hover to cruise and vice versa under the control of a pilot; however, velocity control is not considered. In Ref. (7), velocity control of a tilt-wing aircraft is performed in a wide range of velocity commands using a feedforward controller obtained from wind tunnel testing. However, in the experimental results, there are steady state errors in the velocity response. In Ref. (8), cruise control is validated in experiments for the transition state. It uses a feedforward controller and a feedback controller to track with velocity commands, and shows good performance in the vertical velocity tracking. However, this feedback method has two disadvantages. First, there is a modeling error caused by linearization. Second, the wind disturbance rejection performance is not discussed. To resolve these problems, we propose a novel velocity feedback control in the paper.

**1.3 Contributions of this paper** To solve the above problems, we propose a novel velocity feedback control using a disturbance observer (DOB). DOB was first proposed in the 1980s, and its effectiveness and ease of application have been verified by numerous research in recent years [(9)(10)]. There are some research that applied DOB to a quad-copter [(11)~(13)], however, to the best of the authors' knowledge, no one applied it to velocity control of a tilt-wing eVTOL.

To introduce the wing coordinate system, we can apply the DOB to the tilt-wing eVTOL. It enables us to construct velocity controller easily, and it has a strength in disturbance rejection and decoupling control of thrust force and flap force.

a) Correspondence to: fujimoto@k.u-tokyo.ac.jp
* The University of Tokyo
5-1-5,Kashiwanoha, Kashiwa, Chiba, 227-8561, Japan
** Japan Aerospace Exploration Agency
3-1-1 Yoshinodai, Chuo, Sagamihara, Kanagawa, 252-5210, Japan

Table 1: Parameters definitions.

| Parameter | Definition | Unit |
|---|---|---|
| $\rho$ | air density | kg m$^{-3}$ |
| $D_\mathrm{p}$ | propeller diameter | m |
| $n_\mathrm{p}$ | the number of propeller in the main wing | m |
| $S_a$ | wing area | m$^2$ |
| $S_s$ | wing area in slipstream | m$^2$ |
| $m$ | mass of aircraft | kg |
| $I_b$ | inertia of aircraft around $Y_b$ axis | kg m$^2$ |
| $\omega$ | propeller angular velocity | rad s$^{-1}$ |
| $\delta$ | flap angle | deg |
| $\sigma$ | tilt angle | deg |
| $\alpha$ | angle of attack | deg |
| $\theta_\mathrm{fuselage}$ | pitch angle of aircraft body | rad |
| $\theta_\mathrm{wing}$ | angle between wing and ground | rad |
| $X, Z$ | position of aircraft | m |
| $V_x, V_z$ | velocity of aircraft | m s$^{-1}$ |
| $a_x, a_z$ | acceleration of aircraft | m s$^{-2}$ |
| $\boldsymbol{v}$ | airspeed vector | m s$^{-1}$ |
| $F$ | thrust produced by a propeller | m s$^{-1}$ |
| $\boldsymbol{F}_\mathrm{th}$ | force vector produced by the propeller thrust | N |
| $\boldsymbol{F}_\mathrm{aero}$ | aerodynamic force vector | N |
| $\boldsymbol{F}_\mathrm{w}$ | aerodynamic force vector produced by the wing | N |
| $\boldsymbol{F}_\mathrm{b}$ | aerodynamic force vector produced by the body | N |
| $\boldsymbol{F}_\mathrm{g}$ | gravity vector | N |
| $\boldsymbol{\eta}_F$ | force created by the elevator and the tail-rotor | N |
| $M_\mathrm{th}$ | moment produced by the propeller thrust around $Y_b$ axis | N m |
| $M_\mathrm{w}$ | moment produced by the wing around $Y_b$ axis | N m |
| $\eta$ | moment produced by the elevator and the tail-rotor | N m |
| $(\cdot)_e$ | variables in the earth fixed coordinates | – |
| $(\cdot)_w$ | variables in the wing coordinates | – |
| $(\cdot)_b$ | variables in the body coordinates | – |

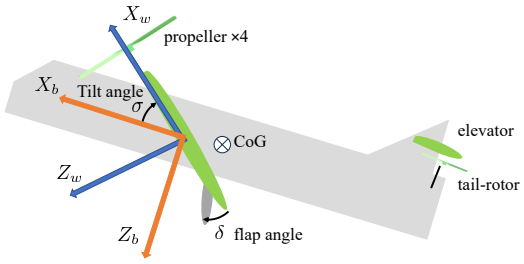


Fig. 1: Model of aircraft.

This idea is an expansion of our previous research on aerodynamic force control system using DOB [4]. We expand it to velocity control for full body system using acceleration measurement. The effectiveness of our proposed method is validated by computer simulations and Hardware-In-the-Loop simulations (HILS) using a wind tunnel. As the first step, this paper only focuses on the longitudinal and translational motions.

## 2. Modeling

**2.1 Equation of motion** Fig. 1 shows the model of the tilt-wing eVTOL used in this paper. It has a main wing whose tilt angle can be changed, an elevator, and a tail-rotor. The main wing has four propellers and two flaps. By controlling the propeller and flap, the forces acting on the aircraft can be changed. The dynamic motion of the aircraft can be expressed by the following equations:

$$m\frac{\mathrm{d}^2}{\mathrm{d}t^2}\begin{bmatrix}X_e\\Z_e\end{bmatrix} = \boldsymbol{F}_\mathrm{th}(\omega) + \boldsymbol{F}_\mathrm{aero}(\omega,\delta) + \boldsymbol{F}_\mathrm{g} + \boldsymbol{\eta}_F, \quad \cdots (1)$$

$$I_b\frac{\mathrm{d}^2}{\mathrm{d}t^2}\theta_\mathrm{fuselage} = M_\mathrm{th}(\omega) + M_\mathrm{aero}(\omega,\delta) + \eta_M. \cdots\cdots (2)$$

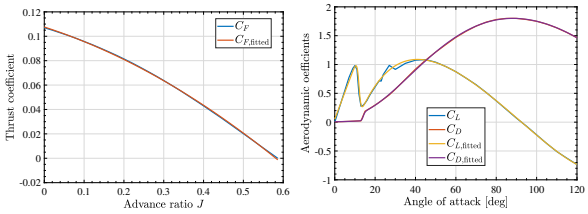


(a) (b)

Fig. 2: Coefficients used in the simulation. (a) Thrust coefficient [14]. (b) Lift and drag coefficients of NACA0012 airfoil [15].

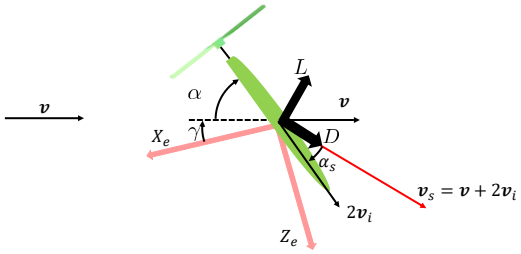


Fig. 3: Diagram of propeller-wing model.

The variables' definition is listed in Table 1. In this paper, it is assumed that the pitch angle of the aircraft is always controlled by an elevator and a tail-rotor to 0 deg, i.e., $\theta_\mathrm{fuselage} = 0$ and the created force by them is small enough. Therefore, only the translational motion is considered. Under this assumption, Eq. (1) can be rewritten as the below equation:

$$m\frac{\mathrm{d}^2}{\mathrm{d}t^2}\begin{bmatrix}X_e\\Z_e\end{bmatrix} = \boldsymbol{F}_\mathrm{th}(\omega) + \boldsymbol{F}_\mathrm{aero}(\omega,\delta) + \boldsymbol{F}_\mathrm{g}. \cdots\cdots (3)$$

$\boldsymbol{F}_\mathrm{aero}(\omega,\delta)$ is aerodynamic force, and it is a sum of forces produced by the wing $\boldsymbol{F}_\mathrm{w}(\omega,\delta)$ and forces produced by the body $\boldsymbol{F}_b$.

**2.2 Propeller model** The thrust generated by the propeller can be calculated using the thrust coefficient $C_F(J)$ as follows:

$$F(J,\omega) = C_F(J)\rho\frac{\omega^2}{4\pi^2}D_\mathrm{p}^4, \cdots\cdots (4)$$

$J$ is the advance ratio defined as $J = \frac{2\pi v_\perp}{\omega D_\mathrm{p}}$. $v_\perp$ is the propeller perpendicular component of the airspeed vector, which is calculated as $v_\perp = v\cos\alpha$, where $\alpha$ is angle of attack. $C_F(J)$ are the function of $J$, and they are fitted from the data provided by Ref. (14) as shown in Fig. 2(a). Using Eq. (4), $\boldsymbol{F}_\mathrm{th}(\omega)$ is calculated as

$$\boldsymbol{F}_\mathrm{th}(\omega) = \begin{bmatrix} n_\mathrm{p}F(J,\omega)\cos\theta_\mathrm{wing} \\ -n_\mathrm{p}F(J,\omega)\sin\theta_\mathrm{wing}\end{bmatrix}, \cdots\cdots (5)$$

where $n_\mathrm{p}$ is the number of propeller in the main wing, and $\theta_\mathrm{wing}$ is an angle between wing and ground.

**2.3 Propeller-wing model** A schematic diagram of the propeller-wing model is shown in Fig. 3. In the figure, $\gamma$ is an angle between ground and airspeed vector $\boldsymbol{v}$. From momentum theory, the induced velocity near the propeller $v_i$ is expressed as

$$v_i = \frac{1}{2}\left(-v_\perp + \sqrt{v_\perp^2 + \frac{2F}{\rho A}}\right) \cdots\cdots (6)$$

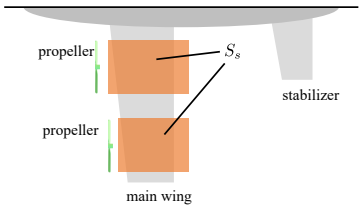

Fig. 4: Wing area in slip stream $S_s$.

where $A$ is the area of a propeller as a disk. Using this expression, the propeller-derived wind speed can be expressed as $2v_i$ based on the momentum theory. By combining with the airspeed $\boldsymbol{v}$, wind velocity acting on the wing $v_s$ and $\alpha_s$ in Fig. 3 can be expressed as

$$v_s = |\boldsymbol{v}_s| = \sqrt{(v\sin\alpha)^2 + (2v_i + v\cos\alpha)^2}, \quad \cdots\cdots (7)$$

$$\alpha_s = \arctan\left(\frac{v\sin\alpha}{2v_i + v\cos\alpha}\right) \cdots\cdots (8)$$

where $\alpha$ is angle of attack expressed as $\alpha = \sigma - \gamma$.

**2.4 Wing model** The forces produced by wing $\boldsymbol{F}_{\mathrm{w}}(\omega, \delta)$ is a sum of the forces produced by the wing with or without the propeller slipstream, i.e., $\boldsymbol{F}_{\mathrm{w}}(\omega, \delta) = \boldsymbol{F}_{\mathrm{w_{s-a}}}(\delta) + \boldsymbol{F}_{\mathrm{w_s}}(\omega, \delta)$. Fig. 4 shows a definition of the area in the slipstream $S_s$. Lift and drag forces produced by the airfoil where is out of the propeller slipstream are calculated as

$$L_{a-s} = \frac{1}{2}C_L(\alpha, \delta)\rho(S_a - S_s)v^2, \cdots\cdots (9)$$

$$D_{a-s} = \frac{1}{2}C_D(\alpha, \delta)\rho(S_a - S_s)v^2 \cdots\cdots (10)$$

where $S_a$ is the area of all airfoil and $S_s$ is the area of airfoil in the propeller slipstream. $C_L$ and $C_D$ called lift coefficients and drag coefficients. In this paper, the lift and drag coefficient is affected by flap angle $\delta$, and modeled as [16]

$$C_L(\alpha, \delta) = C_L(\alpha) + C_{L0}\delta, \cdots\cdots (11)$$

$$C_D(\alpha, \delta) = C_D(\alpha) + C_{D0}\delta^2. \cdots\cdots (12)$$

Experimental data for NACA0012 airfoil at Reynolds number $3.6 \times 10^5$ reported in Ref. (15) is used in computer simulations; whose characteristics are shown in Fig. 2(b).

From Eq. (9) and Eq. (10), $F_{\mathrm{w_{s-a}}}$ is calculated as

$$F_{\mathrm{w_{a-s}}}(\delta) = \begin{bmatrix} -L_{a-s} \\ -D_{a-s} \end{bmatrix}. \cdots\cdots (13)$$

Using the propeller slipstream model shown in Subsection 2.3, the lift and drag forces produced by the airfoil where is in the propeller slipstream are calculated as

$$L_s = \frac{1}{2}C_L(\alpha_s, \delta)\rho S_s v_s^2, \cdots\cdots (14)$$

$$D_s = \frac{1}{2}C_D(\alpha_s, \delta)\rho S_s v_s^2. \cdots\cdots (15)$$

Using Eq. (14) and (15), $F_{\mathrm{w_s}}$ is calculated as

$$F_{\mathrm{w_s}}(\omega, \delta) = \begin{bmatrix} -L_s\sin(\alpha - \alpha_s) - D_s\cos(\alpha - \alpha_s) \\ -L_s\cos(\alpha - \alpha_s) + D_s\cos(\alpha - \alpha_s) \end{bmatrix}. \quad (16)$$

To summarize the above, forces produced by the wing $\boldsymbol{F}_{\mathrm{w}}(\omega, \delta)$ is calculated by the sum of Eq. (13) and Eq. (16).

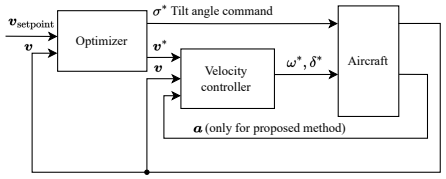

Fig. 5: Translational motion control system of aircraft.

**2.5 Aerodynamic force of the body** The aerodynamic force of the body is modeled as:

$$\boldsymbol{F}_b = \begin{bmatrix} -\frac{1}{2}\rho v_{x_e}|v_{x_e}|S_{\mathrm{body_x}} \\ -\frac{1}{2}\rho v_{z_e}|v_{z_e}|S_{\mathrm{body_z}} \end{bmatrix}, \cdots\cdots (17)$$

where $S_{\mathrm{body_x}}$ and $S_{\mathrm{body_z}}$ are the coefficient that characterizes the body drag force.

## 3. Proposed velocity control system

**3.1 Translational motion control system structure** Translational motion control system of aircraft is shown in Fig. 5. In the figure, optimizer represents the outer layer controller, and it has a role to create the feasible trajectory of tilt angle and velocity against wind conditions when given the velocity set point. The inner layer controller: velocity controller, has a role to track the two-dimensional trajectory using the propeller thrust and flap deflection. We use a propeller and flap because their response is faster than the tilt angle response. This paper focuses on the velocity controller.

**3.2 Conventional method** The conventional velocity controller is shown in Fig. 6 [8]. In Ref. (8), the control allocation based on the following optimization problem is applied:

$$\min_{\boldsymbol{u}^*} (\boldsymbol{J}\boldsymbol{u}^* - \boldsymbol{a}^*)^\top \boldsymbol{W}(\boldsymbol{J}\boldsymbol{u}^* - \boldsymbol{a}^*) + (\boldsymbol{u}^*)^\top \boldsymbol{K}\boldsymbol{u}^*$$
$$\text{s.t. } \boldsymbol{u}^* \in [\boldsymbol{u}_{\min}\ \boldsymbol{u}_{\max}] \cdots\cdots (18)$$

where $\boldsymbol{u}^*$ and $\boldsymbol{J}$ are as follows:

$$\boldsymbol{u}^* = \begin{bmatrix} \Delta\theta_{\mathrm{fuselage}} \\ \Delta\omega \end{bmatrix}, \quad \boldsymbol{J} = \begin{bmatrix} \frac{\partial a_{x_e}}{\partial\theta_{\mathrm{fuselage}}} & \frac{\partial a_{x_e}}{\partial\omega} \\ \frac{\partial a_{z_e}}{\partial\theta_{\mathrm{fuselage}}} & \frac{\partial a_{z_e}}{\partial\omega} \end{bmatrix}. \cdots\cdots (19)$$

The control input allocation as shown in Fig. 6 is derived by setting the regularization matrix $\boldsymbol{K}$ at $\boldsymbol{0}$ and ignoring the constraints of the actuator as a simple implementation. In order to compare the conventional method and proposed method, the pitch angle input is converted to the flap angle. The linearized relationship between acceleration and control input is written as follows:

$$\begin{bmatrix} a_{x_w} \\ a_{z_w} \end{bmatrix} = \boldsymbol{A}\begin{bmatrix} \Delta\omega \\ \Delta\delta \end{bmatrix} \cdots\cdots (20)$$

where $\boldsymbol{A}$ is $2 \times 2$ matrix and its element is a function of airspeed in the $X_b$ direction and $\theta_{\mathrm{wing}}$. $\Delta\omega$ and $\Delta\delta$ are deviations from operating point $\omega_0$, $\delta_0$. The acceleration $\boldsymbol{a}$ is equals to $\boldsymbol{0}$ at the operating point. In the figure, $\boldsymbol{R}$ is a rotational matrix that converts from the earth-fixed coordinate system to the wing coordinate system, which is defined as:

$$\boldsymbol{R}(\theta_{\mathrm{wing}}) = \begin{bmatrix} \cos\theta_{\mathrm{wing}} & -\sin\theta_{\mathrm{wing}} \\ \sin\theta_{\mathrm{wing}} & \cos\theta_{\mathrm{wing}} \end{bmatrix}. \cdots\cdots (21)$$

$C_v$ is PI controller to eliminate steady state errors.

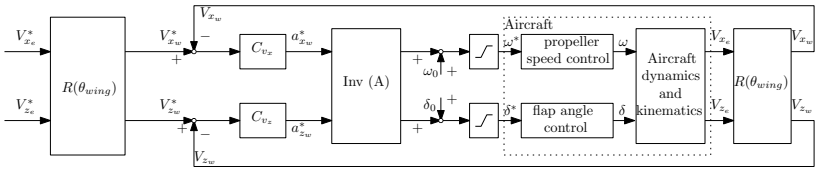


Fig. 6: Conventional velocity control system.

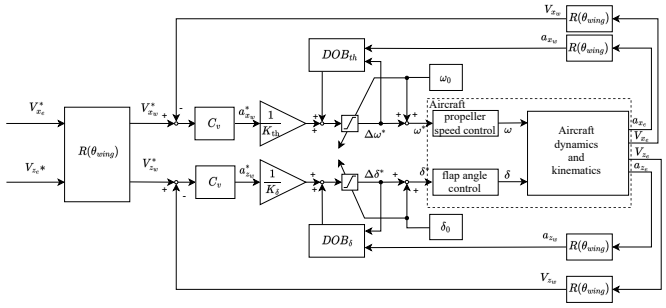


(a) Proposed wing coordinate velocity control system.

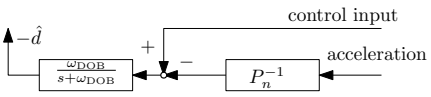


(b) Structure of DOB.

Fig. 7: Proposed wing coordinate velocity control system and structure of DOB

**3.3 Proposed velocity control system** We propose the wing coordinate velocity control system with acceleration-based DOB whose block diagram is shown in Fig. 7(a). The control system is structured so that forces parallel to the wing are controlled by the propellers and forces perpendicular to the wing are controlled by the flaps. This is achieved by decoupling control parallel and perpendicular to the wing by using the DOB with acceleration obtained from an inertial measurement unit (IMU). The plant system can be viewed as a SISO system thanks to the decoupling part, so the control system can be designed easily. In addition, it is possible to compensate high-frequency disturbances and modeling errors by the proposed DOB system.

In the figure, $C_v$ is a proportional controller. The nominal model for each DOB is written as follows:

$$P_{\mathrm{n_{th}}}(s) = \frac{a_{x_w}(s)}{\Delta\omega^*(s)} = \frac{K_{\mathrm{th}}(v_{x_b}, \theta_{\mathrm{wing}})}{\tau_{\mathrm{th}} s + 1}, \quad \cdots\cdots\cdots\cdots (22)$$

$$P_{\mathrm{n}_\delta}(s) = \frac{a_{z_w}(s)}{\Delta\delta^*(s)} = \frac{K_\delta(v_{x_b}, \theta_{\mathrm{wing}})}{\tau_\delta s + 1} \quad \cdots\cdots\cdots\cdots\cdots (23)$$

where $v_{x_b}$ is an airspeed parallel to the body, and we assume that it is obtained from pitot tube. $\tau_{\mathrm{th}}$ and $\tau_\delta$ are the nominal time constant of propeller speed control and flap angle control. $K_{\mathrm{th}}$ and $K_\delta$ is linearized model around operating point:

$$K_{\mathrm{th}} = \left.\frac{\partial a_{x_w}}{\partial \omega}\right|_{\omega=\omega_0, \delta=\delta_0}, \quad K_\delta = \left.\frac{\partial a_{z_w}}{\partial \delta}\right|_{\omega=\omega_0, \delta=\delta_0} \quad \cdots\cdots (24)$$

These are identical to the diagonal term of the matrix $\boldsymbol{A}$, and can be obtained by experiment.

The detailed structure of DOB in this paper is shown in Fig. 7(b). In the figure, $\omega_{\mathrm{DOB}}$ is a cutoff frequency of DOB. It estimates and suppresses the coupling term, the modeling error and the disturbance caused by wind.

## 4. Simulation

We show two simulations to evaluate disturbance rejection performance and decoupling control performance. The aircraft parameters are shown in Table 2. The controller settings are shown in Table 3. The velocity controller is designed by pole placement for the nominal plant $\frac{1}{s}$. The cutoff frequency of the DOB is tuned by trial and error. White Gaussian noise is added to the acceleration measurement. Various values of $\omega$ and $\delta$ are input to the aircraft simulation model, and acceleration $\boldsymbol{a}$ is obtained. $K_{\mathrm{th}}$, $K_\delta$ and matrix $\boldsymbol{A}$ are obtained by linearly approximating the relationships from propeller rotation speed $\omega$ and flap angle $\delta$ to acceleration $a_{x_w}$ and $a_{x_w}$.

Table 2: Aircraft parameter.

| Symbol | Description | Value |
|---|---|---|
| $m$ | mass of aircraft | 2.0 kg |
| – | wingspan | 1.2 m |
| $S_a$ | wing area | 0.30 m$^2$ |
| $S_s$ | wing area in slipstream | 0.25 m$^2$ |
| $D_{\mathrm{p}}$ | propeller diameter | 0.254 m |

Table 3: Controller settings in the simulation.

| Symbol | Description | Value |
|---|---|---|
| – | pole of velocity controller (prop. and conv.) | 2 rad s$^{-1}$ |
| $\tau_{\mathrm{th}}$ | nominal time constant of propeller angular velocity controller | 0.05 s |
| $\tau_\delta$ | nominal time constant of flap angle controller | 0.1 s |
| $\omega_{\mathrm{DOB}}$ | cutoff frequency of DOB | 10 rad s$^{-1}$ |

**4.1 Disturbance rejection** We assume that a situation where the ramp wind disturbance shown in Fig. 8(c) is applied during forward flight at a tilt angle of 3 deg and a velocity command of 11 m s$^{-1}$. Fig. 8 shows the simulation results. It shows that proposed velocity control system can compensate the wind disturbance faster than the conventional method.

**4.2 Decoupling control** In this subsection, the situation where we only control $Z_e$ the direction velocity while the aircraft has the constant speed in $X_e$ the direction is considered. If perpendicular force and parallel force to the wing can be controlled independently, velocity measurement in $X_e$ the direction is a constant value. In this simulation, the tilt angle is set at 50 deg, and the velocity command in the $X$ direction $V^*_{x_e}$ is set at 2 m s$^{-1}$. Fig. 9 shows the simulation

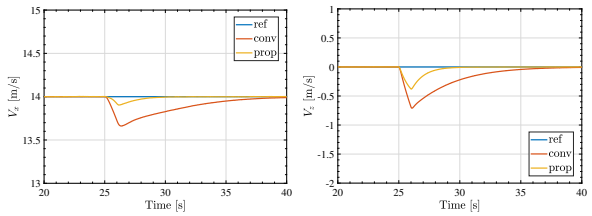


(a) (b)

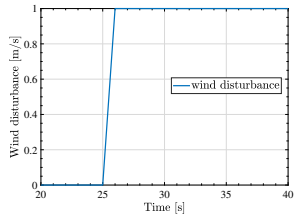


(c)

Fig. 8: The simulation result for performance validation of disturbance rejection. Only one experiment is displayed due to the lack of space. (a) $V_{x_e}$. (b) $V_{z_e}$. (c)Wind disturbance.

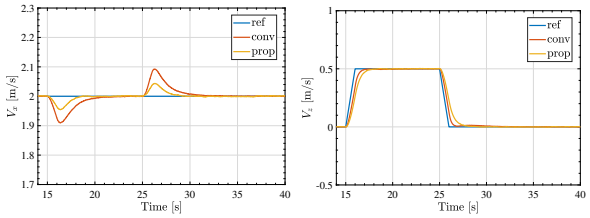


(a) (b)

Fig. 9: The simulation result for performance validation of decoupling control. (a) $V_{x_e}$. (b)$V_{z_e}$.

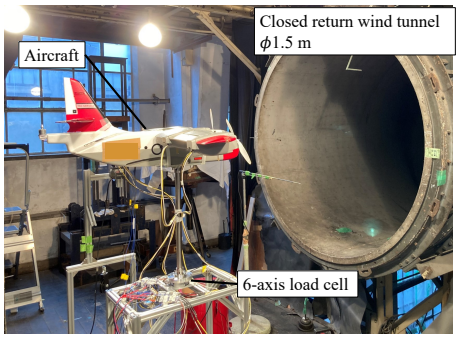


Fig. 10: Experimental setups.

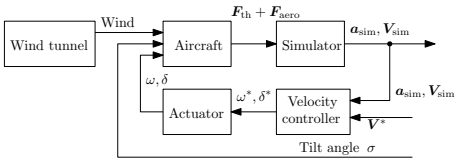


Fig. 11: Block diagram of HILS experiment.

results. In the simulation, proposed method has less error in $V_{x_e}$. It shows that the proposed method has better decoupling performance than the conventional method.

## 5. Experiment

HILS experiment is conducted to validate the proposed method in this section. The experimental setup is shown in Fig. 10. The wind tunnel has a closed return system, whose diameter is 1.5 m. Forces applied to the body are measured with a 6-axis load cell. The actuator command is generated by the controller outside the aircraft.

Table 4: Controller settings in the HILS.

| Symbol | Description | Value |
|---|---|---|
| – | pole of velocity controller (prop. and conv.) | 1.5 rad s$^{-1}$ |
| $\tau_{\text{th}}$ | nominal time constant of propeller angular velocity controller | 0.1 s |
| $\tau_\delta$ | nominal time constant of flap angle controller | 0.063 s |
| $\omega_{\text{DOB}}$ | cutoff frequency of DOB | 3 rad s$^{-1}$ |

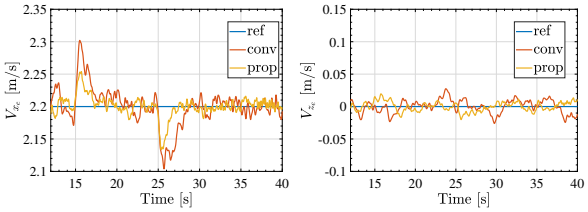


(a) (b)

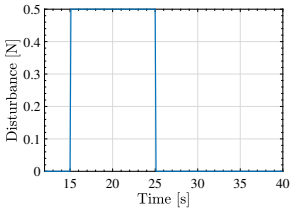


(c)

Fig. 12: The HILS result for performance validation of disturbance rejection. (a) $V_{x_e}$. (b) $V_{z_e}$. (c) Time series of software disturbance in the $X_e$ direction

The block diagram of HILS is shown in Fig. 11. In the simulator block, the calculation is conducted as follows:

$$\boldsymbol{a}_{\text{sim}}(t) = \frac{1}{m}\left(\boldsymbol{F}_{\text{th}} + \boldsymbol{F}_{\text{aero}} + \boldsymbol{F}_{\text{g}}\right), \quad \cdots\cdots\cdots\cdots\cdots (25)$$

$$\boldsymbol{V}_{\text{sim}}(t) = \int_0^t \boldsymbol{a}_{\text{sim}}(\tau)\mathrm{d}\tau. \quad \cdots\cdots\cdots\cdots\cdots\cdots (26)$$

$\boldsymbol{F}_{\text{aero}} + \boldsymbol{F}_{\text{th}}$ is measured with a 6-axis load cell. $\boldsymbol{F}_{\text{g}}$ is a constant value added to load cell measurement because the offset including gravity is removed before measurement. The controller settings in the HILS are shown in Table 4.

**5.1 Disturbance rejection** The situation is the same as the disturbance rejection simulation in Subsection 4.1, however some setting values are different. The tilt angle is set at 60 deg, and the velocity command in the $X$ direction $V^*_{x_e}$ is set at 2.2 m s$^{-1}$. To simulate tailwind disturbance, a software step disturbance of magnitude 0.5 N was applied in the $X_e$ direction. The HILS result is shown in Fig. 12, and RMSE is shown in Table 5. Fig. 12 and Table 5 shows that proposed method has good disturbance rejection performance than conventional method.

**5.2 Decoupling control** The situation is the same as the decoupling control simulation in Subsection 4.2, however some setting values are different. The tilt angle is set at 60 deg, and the velocity command in the $X$ direction $V^*_{x_e}$ is set at 2.2 m s$^{-1}$.

The HILS result is shown in Fig. 13, and RMSE is shown

Table 5: RMSE of velocity in the HILS experiment.

| Experiment | Symbol | Conventional method | Proposed method |
|---|---|---|---|
| Disturbance rejection | $V_{x_e}$ | 0.0335 ± 0.0041 | **0.0166** ± 0.0010 |
| | $V_{z_e}$ | 0.0101 ± 0.0007 | **0.0078** ± 0.0008 |
| Decoupling control w/o modeling error | $V_{x_e}$ | 0.0134 ± 0.0012 | **0.0093** ± 0.0003 |
| | $V_{z_e}$ | **0.0344** ± 0.0010 | 0.0651 ± 0.0010 |
| Decoupling control w/ modeling error | $V_{x_e}$ | 0.0172 ± 0.0008(+28%) | **0.0114** ± 0.0010(+**22**%) |
| (difference from the case w/o modeling error is displayed in %) | $V_{z_e}$ | **0.0430** ± 0.0015(+25%) | 0.0662 ± 0.0003(+**1**%) |

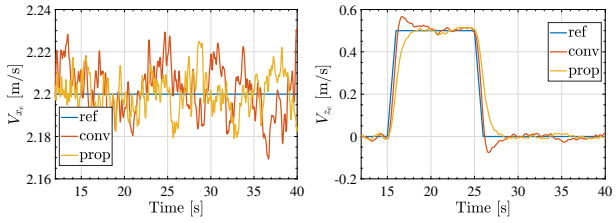


(a) (b)

Fig. 13: The HILS result for performance validation of decoupling control. Only one experiment is displayed due to the lack of space. (a) $V_{x_e}$. (b) $V_{z_e}$.

in Table 5. Table 5 shows that proposed method has less error in the $X_e$ direction than conventional method, and it indicates that proposed method has good disturbance rejection performance. However, the error in the $X_e$ direction of the conventional method is smaller than the error expected from the simulation results. This indicates that the effect of the coupling term is smaller than expected. Therefore, the overshoot that comes from the zero of the PI controller, which is masked by the coupling term's effect in the simulation, becomes apparent in $V_{z_e}$.

To validate the performance of modeling error compensation, the situation that matrix $A$ is set at 20 % larger than that of experimentally obtained. It simulates the change of mass of the aircraft. The RMSE and the RMSE difference between w/ and w/o modeling error is shown in Table 5. It shows that the proposed method has less difference in RMSE in the presence of modeling error, and it indicates that DOB compensate the modeling error.

## 6. Conclusion

We proposed a control system that has strength in easy tuning, disturbance rejection, and decoupling control. By introducing a wing coordinate system and using an acceleration-based disturbance observer, it is possible to consider the control system as two SISO systems. Computer simulation and HILS experiment were conducted to assess the disturbance rejection and decoupling control performance. The simulation and HILS result shows that the proposed method has better performance than the conventional one. Experimental setups will be improved, and an upper layer controller will be built in future work.

## Acknowledgement

Authors would like to thank Professor Kojiro Suzuki, who is the professor of Graduate School of Frontier Sciences, The University of Tokyo for letting us use wind tunnel and giving useful advice. This work was partly supported by JSPS KAKENHI Grant Number JP23H00175.

## References


(1) L. A. Garrow, B. J. German, and C. E. Leonard, "Urban air mobility: A comprehensive review and comparative analysis with autonomous and electric ground transportation for informing future research," *Transportation Research Part C: Emerging Technologies*, vol. 132, p. 103377, 2021.

(2) Y. Tsuji, D. Yashiro, Y. Kato, S. Bando, K. Yubai, and S. Komada, "Design of a thrust controller for propeller driven systems operating at multiple wind velocities and propeller angular velocities," *IEEJ Journal of Industry Applications*, vol. 12, no. 6, pp. 1060–1067, 2023.

(3) K. Yokota and H. Fujimoto, "Pitch angle control by regenerative air brake for electric aircraft," *IEEJ Journal of Industry Applications*, vol. 11, no. 2, pp. 308–316, 2022.

(4) K. Yokota and H. Fujimoto, "Aerodynamic force control for tilt-wing eVTOL using airflow vector estimation," *IEEE Transactions on Transportation Electrification*, vol. 8, no. 4, pp. 4163–4172, 2022.

(5) Y. Naoki, S. Nagai, and H. Fujimoto, "Mode-switching algorithm to improve variable-pitch-propeller thrust generation for drones under motor current limitation," *IEEE/ASME Transactions on Mechatronics*, vol. 28, no. 4, pp. 2003–2011, 2023.

(6) M. Sato and K. Muraoka, "Flight controller design and demonstration of quad-tilt-wing unmanned aerial vehicle," *Journal of Guidance, Control, and Dynamics*, vol. 38, no. 6, pp. 1071–1082, 2015.

(7) P. Hartmann, C. Meyer, and D. Moormann, "Unified velocity control and flight state transition of unmanned tilt-wing aircraft," *Journal of Guidance, Control, and Dynamics*, vol. 40, no. 6, pp. 1348–1359, 2017.

(8) D. Rohr, T. Stastny, S. Verling, and R. Siegwart, "Attitude and cruise control of a vtol tiltwing uav," *IEEE Robotics and Automation Letters*, vol. 4, no. 3, pp. 2683–2690, 2019.

(9) E. Sariyildiz, H. Sekiguchi, T. Nozaki, B. Ugurlu, and K. Ohnishi, "A stability analysis for the acceleration-based robust position control of robot manipulators via disturbance observer," *IEEE/ASME Transactions on Mechatronics*, vol. 23, no. 5, pp. 2369–2378, 2018.

(10) W.-H. Chen, J. Yang, L. Guo, and S. Li, "Disturbance-observer-based control and related methods—an overview," *IEEE Transactions on industrial electronics*, vol. 63, no. 2, pp. 1083–1095, 2015.

(11) X. Lyu, J. Zhou, H. Gu, Z. Li, S. Shen, and F. Zhang, "Disturbance observer based hovering control of quadrotor tail-sitter vtol uavs using $h_\infty$ synthesis," *IEEE Robotics and Automation Letters*, vol. 3, no. 4, pp. 2910–2917, 2018.

(12) Z. Chen, C. Liu, H. Su, X. Liang, and M. Zheng, "A hybrid disturbance observer for delivery drone's oscillation suppression," *Mechatronics*, vol. 88, p. 102907, 2022.

(13) B.-M. Nguyen, T. Kobayashi, K. Sekitani, M. Kawanishi, and T. Narikiyo, "Altitude control of quadcopters with absolute stability analysis," *IEEJ Journal of Industry Applications*, vol. 11, no. 4, pp. 562–572, 2022.

(14) APC prpeller, `https://www.apcprop.com/technical-information/performance-data/`, Accessed 9 Nov. 2023.

(15) R. E. Sheldahl and P. C. Klimas, "Aerodynamic characteristics of seven symmetrical airfoil sections through 180-degree angle of attack for use in aerodynamic analysis of vertical axis wind turbines," tech. rep., Sandia National Laboratories, 1981.

(16) T. Henderson, R. Favour, B. Hamlen, I. Mitha, E. Bowe, and N. Papanikolopoulos, "Hovering locomotion for uavs with thrust-vectoring control surfaces," *IEEE Robotics and Automation Letters*, vol. 7, no. 2, p. 5214–5221, 2022.